*J. Fluid Mech.* (2010), *vol.* 657, *pp.* 430–455. 
doi:10.1017/S0022112010001436

# Steady streaming confined between three-dimensional wavy surfaces

ROMAIN GUIBERT, FRANCK PLOURABOUÉ† AND ALAIN BERGEON

Université de Toulouse; INPT, UPS; IMFT (Institut de Mécanique des Fluides de Toulouse); 1 Allée du Professeur Camille Soula, F-31400 Toulouse, France

CNRS; IMFT; F-31400 Toulouse, France

(Received 17 March 2009; revised 16 March 2010; accepted 16 March 2010)

We present a theoretical and numerical study of three-dimensional pulsatile confined flow between two rigid horizontal surfaces separated by an average gap $h$, and having three-dimensional wavy shapes with arbitrary amplitude $\sigma h$ where $\sigma \sim O(1)$, but long-wavelength variations $\lambda$, with $h/\lambda \ll 1$. We are interested in pulsating flows with moderate inertial effect arising from the Reynolds stress due to the cavity non-parallelism. We analyse the inertial steady-streaming and the second harmonic flows in a lubrication approximation. The dependence of the three-dimensional velocity field in the transverse direction is analytically obtained for arbitrary Womersley numbers and possibly overlapping Stokes layers. The horizontal dependence of the flow is solved numerically by computing the first two pressure fields of an asymptotic expansion in the small inertial limit. We study the variations of the flow structure with the amplitude, the channel's wavelength and the Womersley number for various families of three-dimensional channels. The steady-streaming flow field in the horizontal plane exhibits a quadrupolar vortex, the size of which is adjusted to the cavity wavelength. When increasing the wall amplitude, the wavelengths characterizing the channel or the Womersley number, we find higher-order harmonic flow structures, the origin of which can either be inertially driven or geometrically induced. When some of the channel symmetries are broken, a steady-streaming current appears which has a quadratic dependence on the pressure drop, the amplitude of which is linked to the Womersley number.

## 1. Introduction

Oscillating flows between non-parallel walls display an essential feature associated with nonlinear effects: the existence of a steady-streaming current. As synthetically expressed by Hall (1974), an oscillatory viscous flow over a curved surface sets up a Reynolds stress associated with the oscillatory motion in the Stokes layer. It generates a steady velocity persisting away from the layer because of the viscous effect. The Stokes layer can be induced either by wall or pressure oscillations, and it has been studied for small-amplitude oscillations in various configurations including concentric cylinders (Duck & Smith 1979), parallel plates (Selderov & Stone 2001; Waters 2001) and an elliptical cylinder (Padmanabhan & Pedley 1987). The pulsatile flow in weakly perturbed axisymmetric tubes has been considered (Manton 1971; Grotberg 1984),

† Email address for correspondence: plourab@imft.fr

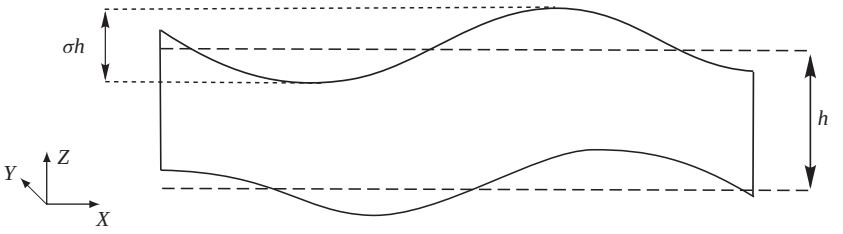


FIGURE 1. Two-dimensional sketch of the parameters and coordinates associated with the wavy surfaces considered. The two bold-faced vertical lines indicate the $X$-positions where a vertically and transversely homogeneous oscillating pressure difference $\Delta P e^{i\omega t}$ is applied.

and the problem has been extended to wavy axisymmetric tubes (Ralph 1986) or non-axisymmetrically perturbed tubes (Ramachandra Rao & Devanathan 1973; Hall 1974). Oscillating flows confined between patterned surfaces have received much attention. Numerical simulations have been used to investigate moderate inertial pulsatile flow in two-dimensional wavy channels (Sobey 1980*a*,*b*; Nishimura *et al.* 1989). Many other studies have been carried out in large inertial regimes exhibiting a wide range of dynamic behaviour. The present work focuses on a moderate inertial effect and is not concerned with the hydrodynamic instabilities that generally appear at large Reynolds number. We rather concentrate on the forced periodic response to an imposed pressure oscillation. Whilst non-inertial flow between elliptic annuli has been recently considered by Gupta, Poulikakos & Kurtcuoglu (2008) in the context of cerebrospinal liquid (CSL), we investigate here the influence of inertial effects due to non-parallelism. The intrathecal space, which is the sheath surrounding the spinal cord, has previously been approximated as the gap between two coaxial cylinders (Gupta *et al.* 2008). However, the ratio of the gap width $h$ to the diameter of the inner cylinder $D$ is small; typically $h/D$ is 1/4 to 1/3. Therefore, in this paper we consider a representation of the gap in which the mean curvature is neglected. The boundaries of the gap are represented by surfaces that deviate around two parallel planes (rather than two concentric cylinders). Hence, developing the azimuthal direction into a transverse Cartesian direction is an interesting approximation to consider.

Some additional curvature effects are similarly neglected, as discussed in § 2. Furthermore, we consider that the ratio of the average gap size $h$ to its spatial longitudinal variations $\lambda$ is small, which is worth considering for intrathecal space in humans, where there are a millimetric gap $h$ and centimetric longitudinal variations $\lambda$, so that $h/\lambda \sim 1/10$ (Nelissen 2008) (this parameter is called $\delta$ by Hall 1974). Furthermore, intrathecal space might display important gap variations, as large as the gap itself, so that at some particular points the cavity is almost closed. Our problem is then associated with a geometry having an average gap $h$, with amplitude variations $\sigma h$ over long-wave distances $\lambda$, with $h/\lambda \ll 1$ and $\sigma \sim O(1)$, as sketched in figure 1.

In this specific context, where inertia is moderate, the reduced Reynolds number $hRe/\lambda$ is less than 1. The reduced Reynolds number is the product of the Reynolds number $Re$, brought about by the applied pressure difference, and the aspect ratio, and will be referred to as a small parameter $hRe/\lambda \ll 1$. However, there is general agreement that the validity range of this approximation covers much broader values of this parameter, i.e. for values as large as $hRe/\lambda \sim 10$, as found by Lo Jacono, Plouraboué & Bergeon (2005).

A second dimensionless quantity, the Womersley number $\alpha$, defined by $\alpha^2 = \omega h^2/(\nu)$, is based on the forcing frequency $\omega$, the viscous relaxation time $h^2/\nu$ related to the

fluid kinematic viscosity $\nu$ and the typical gap $h$. The Womersley number can be either small or large, as in the case of the CSL flow investigated by Gupta *et al.* (2008).

For axisymmetric pipes with small constrictions, the leading-order flow is axisymmetric and can be described by a Womersley-dependent stream function. Successive inertial contributions can then be computed, but they essentially differ in the two limit cases $\alpha \ll 1$ and $\alpha \gg 1$ with $\alpha \ll 1/\sigma$. In the limit of small Womersley numbers, inertial corrections can be estimated everywhere inside the pipe using a regular expansion in $\alpha$, whereas in the large-Womersley-number regime, a Stokes layer of thickness $\sim 1/\alpha$ develops near the pipe walls (Hall 1974; Grotberg 1984). In this case, it is necessary to match the Stokes layer with the outer core region, which then separates the steady-streaming contribution into two distinct regions.

In this paper we improve the analysis of weakly inertial pulsatile flows in two ways. Firstly, we extend the class of geometries because we only require the gap of the channel to have long-wavelength variations. In particular, our results do not only apply to variations of small amplitude. Therefore, our analysis applies to a large number of configurations, including those encountered in cerebrospinal flow around the spinal cord, for which the flow is confined along one direction with possibly local arbitrarily small gaps, whilst spatial variations in the other two directions occur over a similar long-wavelength $\lambda$ under the assumption that $h/\lambda \ll 1$. Hence, as opposed to previous works where the two geometrical parameters $\sigma$ and $\epsilon$ were assumed to be small, only $\epsilon$ is considered small here. Within this lubrication constraint, any arbitrary aperture variation is potentially addressed. One unavoidable outcome of such a general framework is the necessity for some numerical computation to solve the leading-order lubrication flow and any further inertial perturbation. Our analysis, however, shows that the numerical cost is only that of solving a stationary two-dimensional Poisson problem and it is a drastic simplification of the initial three-dimensional time-dependent problem with, possibly, thin Stokes layers inside the gap thickness.

Secondly, we address the computation of the steady-streaming flow associated with either a small or a large Womersley number within the same formulation, so that any arbitrary intermediate value (most physiologically meaningful values are indeed for $\alpha$ within the range 0.5–3) can be covered by our formulation. This goal is different from that previously achieved by Hall (1974) and Grotberg (1984) since we avoid solving the inner and outer Stokes layer regions separately. Our analytical solution captures both regions inside the gap, which is a nice feature of the approach when Stokes layers overlap for Womersley numbers of order 1.

The paper is organized as follows. The dimensionless formulation and the governing equations are introduced in § 2. An asymptotic analysis of the flow in the weak inertia regime is performed in § 3. This analysis brings to the fore a boundary layer type of pressure field which is uniform along the vertical direction and has horizontal variations necessitating some two-dimensional numerical computation, as described in § 4. These pressure numerical computations allow the complete velocity field to be reconstructed, some examples of which are shown in § 5. Finally, the global pressure–flux relation is analysed in greater detail in § 5.2.2.

## 2. Governing equations

We study the incompressible flow between two rigid surfaces defined by $\mathrm{z} - \mathrm{z}_1(\mathrm{x}, \mathrm{y}) = \mathrm{z} - \mathrm{z}_2(\mathrm{x}, \mathrm{y}) = 0$. Here x and y are defined as the horizontal coordinates

and z as the vertical coordinate (although gravity is neglected). We introduce the aperture $\Delta z = z_2 - z_1$ and assume that $\Delta z > 0$. The two functions $z_1$ and $z_2$ are smooth continuous $\lambda$-periodic functions of x and y and we introduce the aspect ratio $\epsilon = 2\pi h/\lambda$, where $h$ is the averaged aperture.

The horizontal lengths are non-dimensionalized with $\lambda/2\pi$ and the transverse (vertical) length with $h$. Hereafter, dimensionless lengths $X = 2\pi x/\lambda$, $Y = 2\pi y/\lambda$ and $z = z/h$ will be used to reinforce the fact that the two scales differ by $\epsilon$. The unscaled vertical coordinate $Z = 2\pi z/\lambda$ is thus $Z = \epsilon z$. For numerical convenience associated with the computations of §4, we set $\max(X, Y) = 2\pi$, whereas $z \sim O(1)$. The flow is driven by an imposed pressure difference in the $X$ direction oscillating periodically in time. Its amplitude $\Delta P$ is used to build the dimensionless pressure $p$ and its period of oscillation $1/\omega$ is used for the dimensionless time. The horizontal velocity components are scaled by a viscous velocity $v_\mu = 2\pi h^2 \Delta P/\mu\lambda$ based on the applied pressure gradient, where $\mu$ is the dynamic viscosity. Because of the incompressibility constraint and the different scaling in space, the vertical component of the velocity is non-dimensionalized by $\epsilon v_\mu = (2\pi)^2 h^3 \Delta P/\mu\lambda^2$. This dimensionless formulation brings to the fore the lubrication Reynolds number $\epsilon Re = \epsilon\ ((2\pi)h^2\Delta P/\mu\lambda)\ (h\rho/\mu) = (2\pi)^2\rho\Delta P h^4/\mu^2\lambda^2$ and the Womersley number $\alpha$ defined by $\alpha^2 = \omega h^2/\nu$. Note that $\epsilon Re$ and $\alpha$ are free parameters and can be independently assigned to a prescribed value. Using $t$, $p$ and $\mathscr{U} = (u, v, \epsilon w)$ for the dimensionless time, pressure and velocity, respectively, and neglecting $O(\epsilon^2, \epsilon^3 Re, \epsilon^2\alpha^2)$ terms, body forces and gravity effects, the dimensionless Navier–Stokes equations read

$$\left.\begin{aligned} \alpha^2\,\partial_t u + \epsilon Re\left(u\frac{\partial u}{\partial X} + v\frac{\partial u}{\partial Y} + w\frac{\partial u}{\partial z}\right) &= -\frac{\partial p}{\partial X} + \frac{\partial^2 u}{\partial z^2}, \\ \alpha^2\,\partial_t v + \epsilon Re\left(u\frac{\partial v}{\partial X} + v\frac{\partial v}{\partial Y} + w\frac{\partial v}{\partial z}\right) &= -\frac{\partial p}{\partial Y} + \frac{\partial^2 v}{\partial z^2}, \\ 0 &= -\frac{\partial p}{\partial z}. \end{aligned}\right\} \tag{2.1}$$

The incompressibility constraint gives

$$\frac{\partial u}{\partial X} + \frac{\partial v}{\partial Y} + \frac{\partial w}{\partial z} = 0. \tag{2.2}$$

No-slip boundary conditions are used along the two channel boundaries defined by $z - z_1(X, Y) = 0$ and $z - z_2(X, Y) = 0$. This gives

$$\mathscr{U}(X, Y, z = z_1) = \mathscr{U}(X, Y, z = z_1) = 0, \tag{2.3}$$

where $z_1$ and $z_2$ stand for the dimensionless version of $z_1$ and $z_2$. The set of equations (2.2)–(2.3) are, however, difficult to use with the asymptotic sequence developed below, which is well known in lubrication theory. This is because boundary conditions (2.3) give two independent conditions to be satisfied, while the incompressibility condition (2.2) to be considered for solving the third component of velocity $w$ just requires one condition when the first-order derivative of $w$ is integrated. This difficulty can be overcome by considering a suitable coordinate system, which proves to be as simple to use as Cartesian coordinates in a long-wavelength asymptotic analysis. An interesting improvement can then be obtained in the following analysis, when it is understood that the boundary conditions can be transformed into a single antisymmetric condition in

a deformed coordinate system,

$$z_\pm = \tfrac{1}{2}(z_2 \pm z_1), \qquad \hat{z} = z - z_+. \tag{2.4}$$

In the new coordinates $(X, Y, \hat{z})$, boundary condition (2.3) takes the form of a symmetric condition,

$$\mathscr{U}(X, Y, \hat{z} = \pm z_-) = 0, \tag{2.5}$$

which is now consistent with the single condition needed to find the third velocity component $w$. Nevertheless, in this new non-orthogonal coordinate set $(X, Y, \hat{z})$, the governing equations are changed by additional terms. The asymptotic Navier–Stokes equations (2.1) now read

$$\left.\begin{aligned}
\alpha^2\partial_t u + \epsilon Re\left(u\frac{\partial u}{\partial X} - u\frac{\partial z_+}{\partial X}\frac{\partial u}{\partial \hat{z}} + v\frac{\partial u}{\partial Y} - v\frac{\partial z_+}{\partial Y}\frac{\partial u}{\partial \hat{z}} + w\frac{\partial u}{\partial \hat{z}}\right) &= -\frac{\partial p}{\partial X} + \frac{\partial z_+}{\partial X}\frac{\partial p}{\partial \hat{z}} + \frac{\partial^2 u}{\partial \hat{z}^2},\\
\alpha^2\partial_t v + \epsilon Re\left(u\frac{\partial v}{\partial X} - u\frac{\partial z_+}{\partial X}\frac{\partial v}{\partial \hat{z}} + v\frac{\partial v}{\partial Y} - v\frac{\partial z_+}{\partial Y}\frac{\partial v}{\partial \hat{z}} + w\frac{\partial v}{\partial \hat{z}}\right) &= -\frac{\partial p}{\partial Y} + \frac{\partial z_+}{\partial Y}\frac{\partial p}{\partial \hat{z}} + \frac{\partial^2 v}{\partial \hat{z}^2},\\
0 &= -\frac{\partial p}{\partial \hat{z}},
\end{aligned}\right\} \tag{2.6}$$

and the incompressibility condition has to be written as

$$\frac{\partial u}{\partial X} - \frac{\partial z_+}{\partial X}\frac{\partial u}{\partial \hat{z}} + \frac{\partial v}{\partial Y} - \frac{\partial z_+}{\partial Y}\frac{\partial v}{\partial \hat{z}} + \frac{\partial w}{\partial \hat{z}} = 0. \tag{2.7}$$

To complete these governing equations additional boundary conditions are required on the horizontal boundaries ($(X, Y)$ plane) of the domain. As mentioned in the Introduction, we assume that a pressure difference is imposed in the $X$ direction. In this study a number of boundary conditions are considered. Either a constant pressure along the boundaries $X = 0$ and $X = 2\pi$ is prescribed for a finite cavity, or some periodic boundary conditions are applied for an infinite set of periodic cavities. Similarly, for lateral boundary conditions along $Y = 0$ and $Y = 2\pi$, we consider the case of a finite cavity or an infinite set of periodic cavities, as further detailed in § 4.1.

## 3. Asymptotic analysis

Below, we follow Hall (1974) and Lo Jacono *et al.* (2005) and perform a weak-inertia expansion to find an approximate flow field including inertial steady streaming. We begin by setting

$$[p, \mathscr{U}] = [p_0, \mathscr{U}_0] + \epsilon Re\,[p_1, \mathscr{U}_1] + O(\epsilon^2 Re^2), \tag{3.1}$$

where we consider that $\epsilon \ll \epsilon Re \ll 1$. Effects of order $O(\epsilon)$ are not considered in the asymptotic sequence since they do not lead to any corrections to the lubrication leading order (Leal 1992). However, the Womersley number $\alpha$ can be larger than unity up to the constraint $\epsilon^2\alpha^2 \ll 1$ as well as $\alpha^2 \ll Re/\epsilon$, as discussed in § 6.1. Nevertheless, the latter is the only relevant constraint since it implies the former in the limit $\epsilon Re \ll 1$. The leading-order term is the lubrication approximation of the flow and is a local adaptation of the Stokes solution, as discussed in the next subsection. The next-order term is the weak inertial correction and has been computed at the stationary limit ($\alpha = 0$) by Lo Jacono *et al.* (2005). In the following, the horizontal flux $\boldsymbol{q}$ is also introduced as

$$\boldsymbol{q} = \int_{z_1}^{z_2} \boldsymbol{u}\,\mathrm{d}z = \int_{-z_-}^{z_-} \boldsymbol{u}\,\mathrm{d}\hat{z}, \tag{3.2}$$

where $\boldsymbol{u}=(u, v)$ refers to the two-dimensional horizontal velocity field. In § 5.2.2 we will investigate the relationship between the total flux in the longitudinal direction and the applied pressure difference. For this purpose, the total flux $\boldsymbol{Q}$ is defined by

$$\boldsymbol{Q}=\int_0^{2\pi}\boldsymbol{q}\ \mathrm{d}Y. \tag{3.3}$$

Because of the boundary conditions, $\boldsymbol{Q}$ is in the direction of the applied pressure gradient so that $\boldsymbol{Q}=(Q, 0)$.

### 3.1. *Lubrication solution*

Introducing the asymptotic expansion (3.1) in equations (2.6) gives, to leading order, the lubrication equations

$$\alpha^2\frac{\partial \boldsymbol{u}_0}{\partial t}=-\nabla p_0+\nabla z_+\frac{\partial p_0}{\partial \hat{z}}+\frac{\partial^2 \boldsymbol{u}_0}{\partial \hat{z}^2},\quad 0=-\frac{\partial p_0}{\partial \hat{z}}, \tag{3.4}$$

where $\nabla\equiv(\partial_X, \partial_Y)$ stands for the two-dimensional horizontal components of the gradient.

We next work with complex numbers and introduce the complex fields $\tilde{p}_0$, $\tilde{\mathscr{U}}_0$ and $\tilde{\boldsymbol{q}}_0$ such that

$$[p_0, \mathscr{U}_0, \boldsymbol{q}_0]=\Re\left\{\left[\tilde{p}_0, \tilde{\mathscr{U}}_0, \tilde{\boldsymbol{q}}_0\right]\mathrm{e}^{\mathrm{i}t}\right\}, \tag{3.5}$$

since the boundary conditions are time-periodic and the equations are linear at this stage. Moreover, since $p_0$ does not depend on $\hat{z}$, (3.4) leads to the following linear problem:

$$\frac{\partial^2 \tilde{\boldsymbol{u}}_0}{\partial \hat{z}^2}-\mathrm{i}\alpha^2\tilde{\boldsymbol{u}}_0-\nabla\tilde{p}_0=0. \tag{3.6}$$

The solution is found to be

$$\tilde{\boldsymbol{u}}_0=\frac{\nabla\tilde{p}_0}{k^2}\left(\frac{\cosh(k\hat{z})}{\cosh(kz_-)}-1\right), \tag{3.7a}$$

$$k=\alpha\sqrt{\mathrm{i}}. \tag{3.7b}$$

It can be seen that this solution is the trivial extension of the known Stokes solution for pulsatile flow between parallel planes obtained by replacing the uniform gap separation by the local gap $z_-(X, Y)$.

From this, we find the horizontal flux $\boldsymbol{q}$ and the associated complex hydraulic conductance $K_0$:

$$\tilde{\boldsymbol{q}}_0=-K_0\nabla\tilde{p}_0, \tag{3.8a}$$

$$K_0=-\frac{2}{k^3}\left(\tanh(kz_-)-kz_-\right), \tag{3.8b}$$

where the leading-order pressure $\tilde{p}_0$ solves the two-dimensional problem,

$$\nabla\cdot\tilde{\boldsymbol{q}}_0=\nabla\cdot(K_0\nabla\tilde{p}_0)=K_0\nabla^2\tilde{p}_0+\frac{\mathrm{d}K_0}{\mathrm{d}z_-}\nabla z_-\cdot\nabla\tilde{p}_0=0. \tag{3.9}$$

Finally the third component of the velocity is obtained from the integration of the incompressibility condition (2.7) and expression (3.9). We find

$$\tilde{w}_0=\tilde{w}_0^+ + \tilde{w}_0^-, \tag{3.10a}$$

$$\tilde{w}_0^+=\nabla z_+\cdot\boldsymbol{u}_0, \tag{3.10b}$$

$$\tilde{w}_0^- = -\frac{\nabla^2 \tilde{p}_0}{k^2}\left(\frac{z_- \sinh(k\hat{z})}{\sinh(kz_-)} - \hat{z}\right), \tag{3.10c}$$

where the third component of the velocity $\tilde{w}_0$ was decomposed into a sinuous contribution $\tilde{w}_0^+$ (which is zero when $z_+$ is constant) and a varicose term $\tilde{w}_0^-$ (which is zero when $z_-$ is constant, because, in this case, $K_0$ is constant and from (3.9), $\tilde{p}_0$ harmonic). In relation (3.10*c*), $\nabla^2$ is the two-dimensional Laplacian in the $X$ and $Y$ coordinates.

### 3.2. *First inertial correction*

The next order of expansion (3.1) in (2.6) leads to a similar Stokes problem for the inertial perturbation

$$\begin{aligned} \alpha^2 \frac{\partial \boldsymbol{u}_1}{\partial t} + \boldsymbol{u}_0 \cdot \nabla \boldsymbol{u}_0 - (\boldsymbol{u}_0 \cdot \nabla z_+)\frac{\partial \boldsymbol{u}_0}{\partial \hat{z}} + w_0 \frac{\partial \boldsymbol{u}_0}{\partial \hat{z}} &= -\nabla p_1 + \nabla z_+ \frac{\partial p_1}{\partial \hat{z}} + \frac{\partial^2 \boldsymbol{u}_1}{\partial \hat{z}^2}, \\ 0 &= -\frac{\partial p_1}{\partial \hat{z}}. \end{aligned} \tag{3.11}$$

The first inertial pressure perturbation is still invariant in the $\hat{z}$ direction and therefore extends the boundary-layer property of the leading-order lubrication pressure (this proves to be the case at the next $O((\epsilon Re)^2)$ order). Because of the nonlinear interaction between the first-order terms in relation (3.11), a non-zero time-independent term and a nonlinear harmonic response oscillating as $\exp(2it)$ appear in the asymptotic expansion of the first corrections. We therefore seek $[p_1, \mathscr{U}_1, \boldsymbol{q}_1]$ as

$$[p_1, \mathscr{U}_1, \boldsymbol{q}_1] = \tfrac{1}{2}\,[p_{1s}, \mathscr{U}_{1s}, \boldsymbol{q}_{1s}] + \tfrac{1}{2}\Re\{[\tilde{p}_{1u}, \tilde{\mathscr{U}}_{1u}, \tilde{\boldsymbol{q}}_{1u}]\mathrm{e}^{2it}\}, \tag{3.12}$$

where subscripts $s$ and $u$ refer to the stationary and time-dependent parts. The 1/2 prefactor on the right-hand side of (3.12) is set to find a consistent asymptotic steady limit $\alpha \to 0$ to the stationary solution.

#### 3.2.1. *Steady streaming*

Inserting (3.5) and (3.12) in (3.11), we see that the steady part of (3.12) solves

$$\frac{\partial^2 \boldsymbol{u}_{1s}}{\partial \hat{z}^2} - \nabla p_{1s} = \frac{1}{2}\left(\tilde{\boldsymbol{u}}_0 \cdot \nabla \tilde{\boldsymbol{u}}_0^* + \tilde{w}_0^- \frac{\partial \tilde{\boldsymbol{u}}_0^*}{\partial \hat{z}} + \text{c.c.}\right), \tag{3.13}$$

where the sinuous contribution associated with the third component of the velocity $\tilde{w}_0^+$ in the right-hand side Navier term exactly cancels out the Reynolds stress associated with the coordinate change $-(\tilde{\boldsymbol{u}}_0 \cdot \nabla z_+)(\partial \tilde{\boldsymbol{u}}_0/\partial \hat{z})$. Since the pressure gradient does not depend on $\hat{z}$ and since the $\hat{z}$-variations of the right-hand side of (3.13) are analytically known from (3.7) and (3.10), the solution can be written as

$$\boldsymbol{u}_{1s} = F_{1s}\nabla p_{1s} + F_{2s}\nabla\left(\nabla \tilde{p}_0 \cdot \nabla \tilde{p}_0^*\right) + \left[(F_{3s} + F_{4s})\nabla \tilde{p}_0^*\,(\nabla \tilde{p}_0 \cdot \nabla z_-) + \text{c.c.}\right], \tag{3.14}$$

where both $*$ and c.c. stand for complex conjugate ($\boldsymbol{u}_{1s}$ is real). The functions $F_{is}$, $i = 1, 4$ are reported in the Appendix. The first term $F_{1s}$ is associated with the stationary inertial pressure gradient correction. It displays the expected parabolic profile since it is associated with a stationary flow. All functions $F_{is}$ fulfil the no-slip boundary conditions (2.5). The variations of the three functions $F_{is}$ ($i = 2, 3, 4$) with the Womersley number $\alpha$ are non-trivial. Note, however, that at the stationary limit $\alpha, k \to 0$ ($k$ is directly related to $\alpha$ by relation (3.7*b*)), we recover the polynomial dependence with $\hat{z}$ obtained by Lo Jacono *et al.* (2005) in identical geometries but stationary pressure gradient. As opposed to previous analysis by Hall (1974) and

Grotberg (1984) in which the large- or small-Womersley-number limits are discussed separately with specific asymptotic approaches, our results (3.14) and (A 1) offer a complete representation of the steady-streaming solution valid for a large range of Womersley number $\alpha$, and possibly overlapping Stokes layers.

Integrating the functions $F_{is}$ in the $\hat{z}$ direction, we also obtain the steady part of the velocity flux correction

$$\boldsymbol{q}_{1s} = -K_{1s}\nabla p_{1s} + G_{2s}\nabla(\nabla\tilde{p}_0\cdot\nabla\tilde{p}_0^*) + ((G_{3s}+G_{4s})\nabla\tilde{p}_0^*\cdot(\nabla\tilde{p}_0\cdot\nabla z_-) + \text{c.c.}), \tag{3.15}$$

where the first term of the right-hand side associated with a hydraulic conductance $K_{1s} = 2z_-^3/3$ balances the stationary inertial pressure gradient $\nabla p_{1s}$. Functions $G_{is}$ are obtained from the integration (3.2) of the $F_{is}$ functions given in (A 1) and read

$$\left.\begin{aligned}
G_{2s} &= \frac{1}{k^4}\left(\frac{z_-^3}{3} + \frac{z_-\tanh(kz_-)\tanh(k^*z_-)}{2kk^*} + \frac{5}{4k^2}\left(\frac{\tanh(kz_-)}{k} - \frac{\tanh(k^*z_-)}{k^*}\right)\right),\\
G_{3s} &= -\frac{\tanh(k^*z_-)}{\alpha^4}\left(\frac{\sqrt{\mathrm{i}}z_-}{\alpha}\left(1 + \frac{\mathrm{i}\tanh(kz_-)\tanh(k^*z_-)}{2}\right)\right.\\
&\qquad\left. + \frac{\tanh(kz_-) - 5\mathrm{i}\tanh(k^*z_-)}{4\alpha^2}\right),\\
G_{4s} &= \frac{z_-\tanh(kz_-)}{k^3[kz_-\cosh(kz_-) - \sinh(kz_-)]}\left(\frac{z_-\cosh(kz_-)}{2k} - \frac{13\sinh(kz_-)}{4k^2}\right.\\
&\qquad\left. - \frac{\tanh(k^*z_-)}{k^*}\cdot\left[z_-\sinh(kz_-) + \frac{\cosh(kz_-)}{4k} - \frac{3\sinh(kz_-)}{k^2z_-}\right]\right).
\end{aligned}\right\} \tag{3.16}$$

3.2.2. *Nonlinear harmonic response*

A similar forced Stokes problem is obtained for the time-dependent inertial velocity

$$\frac{\partial^2\tilde{\boldsymbol{u}}_{1u}}{\partial\hat{z}^2} - 2\mathrm{i}\alpha^2\tilde{\boldsymbol{u}}_{1u} - \nabla\tilde{p}_{1u} = \tilde{\boldsymbol{u}}_0\cdot\nabla\tilde{\boldsymbol{u}}_0 + \tilde{w}_0^-\frac{\partial\tilde{\boldsymbol{u}}_0}{\partial\hat{z}}. \tag{3.17}$$

We obtain a similar velocity–pressure relation

$$\tilde{\boldsymbol{u}}_{1u} = F_{1u}\nabla\tilde{p}_{1u} + F_{2u}\nabla(\nabla\tilde{p}_0)^2 + (F_{3u}+F_{4u})\nabla\tilde{p}_0(\nabla\tilde{p}_0\cdot\nabla z_-), \tag{3.18}$$

where, as expected, the first term $F_{1u}$ balancing the oscillating pressure gradient $\nabla\tilde{p}_{1u}$ is simply a replica of the Stokes solution (3.7) with a rescaled parameter $\sqrt{2}k = \sqrt{2}\alpha\sqrt{\mathrm{i}}$ associated with the prefactor $\exp(2\mathrm{i}t)$. The functions $F_{iu}$ fulfil the correct boundary conditions and their stationary limit is consistent with the polynomial expansion obtained by Lo Jacono *et al.* (2005). It is then possible to obtain the period-2 oscillating flux–pressure

$$\tilde{\boldsymbol{q}}_{1u} = -K_{1u}\nabla p_{1u} + G_{2u}\nabla(\nabla\tilde{p}_0)^2 + (G_{3u}+G_{4u})\nabla\tilde{p}_0(\nabla\tilde{p}_0\cdot\nabla z_-), \tag{3.19}$$

where

$$\left.\begin{aligned}
K_{1u} &= -\frac{\sqrt{2}}{2k^3}\left(\tanh[\sqrt{2}kz_-] - \sqrt{2}kz_-\right),\\
G_{2u} &= \frac{1}{4k^6}\left(\left(\frac{1}{\cosh^2(kz_-)}-4\right)\left(\frac{\sqrt{2}\tanh(\sqrt{2}kz_-)}{k}-z_-\right)+\frac{9\tanh(kz_-)}{k}-6z_-\right),\\
G_{3u} &= \frac{\tanh(kz_-)}{2k^6}\left(\frac{kz_-}{\cosh^2(kz_-)}-5\tanh(kz_-)+\sqrt{2}\tanh(\sqrt{2}kz_-)\left(3-\frac{1}{\cosh^2(kz_-)}\right)\right),\\
G_{4u} &= \frac{z_-\tanh(kz_-)}{2k^5[kz_-\cosh(kz_-)-\sinh(kz_-)]}\left(\sqrt{2}\tanh(\sqrt{2}kz_-)\left(\frac{2}{\cosh(kz_-)}-\sinh(kz_-)\right.\right.\\
&\qquad\left.\left.\cdot\left[\frac{3}{\tanh(kz_-)}+\frac{4}{kz_-}\right]\right)+\frac{kz_-}{\cosh(kz_-)}+\sinh(kz_-)\left[5+\frac{4\tanh(kz_-)}{kz_-}\right]\right).
\end{aligned}\right\} \tag{3.20}$$

The first term $K_{1u}$ is the oscillating hydraulic conductance which is a replica of the leading-order conductance (3.8*b*) after substituting the parameter $k$ with $\sqrt{2}k$. As in the previous subsection, the functions $G_{iu}$ are the integrals (3.2) of functions $F_{iu}$ in equations (A 2).

Finally, the equations governing the leading-order pressure $\tilde{p}_0$ and first-order pressures $\tilde{p}_{1s}$ and $\tilde{p}_{1u}$ are

$$\nabla^2\tilde{p}_0 + \frac{k\tanh^2(kz_-)}{kz_- - \tanh(kz_-)}\nabla z_-\cdot\nabla\tilde{p}_0 = 0, \tag{3.21a}$$

$$\nabla^2\tilde{p}_{1s} + \frac{3}{z_-}\nabla z_-\cdot\nabla\tilde{p}_{1s} = f_{1s}[\tilde{p}_0], \tag{3.21b}$$

$$\nabla^2\tilde{p}_{1u} + \frac{\sqrt{2}k\tanh^2(\sqrt{2}kz_-)}{\sqrt{2}kz_- - \tanh(\sqrt{2}kz_-)}\nabla z_-\cdot\nabla\tilde{p}_{1u} = f_{1u}[\tilde{p}_0], \tag{3.21c}$$

where expressions for functions $f_{1s}$, $f_{1u}$ can be found by imposing the incompressibility conditions on flux (3.15) and (3.19) whilst using relations (3.16) and (3.20). Equations (3.21) are then solved numerically.

## 4. Numerical computations

The results obtained in the previous section give explicit analytical expressions for the $\hat{z}$-variations of the lubrication leading order and its first-order inertial velocity correction. Examination of relations (3.7), (3.14) and (3.18) shows that the complete expressions for the velocity fields require the evaluation of the pressure fields $p_0$, $p_{1s}$ and $p_{1u}$ in the $(X, Y)$ plane.

Using the incompressibility equation (2.2), the no-slip velocity boundary conditions along the two surfaces $z = \pm z_-$ and expansion (3.12), it is straightforward to obtain

$$\nabla\cdot\tilde{\boldsymbol{q}}_0 = \nabla\cdot\boldsymbol{q}_{1s} = \nabla\cdot\tilde{\boldsymbol{q}}_{1u} = 0. \tag{4.1}$$

Therefore, the pressure fields $p_0$, $p_{1s}$ and $p_{1u}$ are each a solution of a Poisson problem arising from the incompressibility constraints (4.1) of the corresponding velocity fluxes (3.8), (3.15) and (3.19). These two-dimensional problems are solved numerically and the numerical procedure is described below. Different pressure and velocity boundary conditions are discussed depending on the application to be considered.

### 4.1. *Boundary conditions*

The $(X, Y)$ domain is chosen as either the square $[0, 2\pi] \times [0, 2\pi]$ or the rectangle $[0, \pi] \times [0, 2\pi]$. We consider three types of boundary conditions for the pressure field, corresponding to physically different situations.

With the first set of boundary conditions, we consider a domain bounded at $Y = 0$ and $Y = 2\pi$ by rigid walls along which Neumann boundary conditions are imposed for the pressure. This is a usual procedure in Hele-Shaw cell configurations. The true no-slip boundary condition along $Y = 0$ and $Y = 2\pi$ is accommodated in a small region of size $h$ near the rigid walls. This procedure avoids solving the three-dimensional Stokes flow localized along the lateral edges of a confined cavity and does not take into account the lateral viscous boundary layer, known to have a small impact in such a confined system. This case is particularly interesting for domains with a finite extension in the transverse direction, such as the textured channel studied by Stroock *et al.* (2002). In the $X$ direction, a periodically oscillating pressure gradient is imposed and created by prescribed pressure values at the boundaries $X = 0$ and $X = 2\pi$ (or $X = \pi$). In terms of amplitude, the boundary conditions read as

$$\mathscr{D}: \quad p(0, Y) = p(2\pi, Y) - 1 = 0, \tag{4.2a}$$

$$\mathscr{N}: \quad \frac{\partial p}{\partial Y}(X, 0) = \frac{\partial p}{\partial Y}(X, 2\pi) = 0. \tag{4.2b}$$

Boundary conditions (4.2) are Dirichlet–Neumann and referred to as $\mathscr{D}/\mathscr{N}$ hereafter. Inserting decomposition (3.1) in (4.2) leads to the same set of boundary conditions for the leading-order lubrication pressure $p_0$ except for a non-zero pressure Dirichlet condition

$$\mathscr{D}: \quad \tilde{p}_i(0, Y) = \tilde{p}_i(2\pi, Y) - d_i = 0, \tag{4.3a}$$

$$\mathscr{N}: \quad \frac{\partial \tilde{p}_i}{\partial Y}(X, 0) = \frac{\partial \tilde{p}_i}{\partial Y}(X, 2\pi) = 0, \tag{4.3b}$$

where $i = 0, 1$, $d_0 = 1$ and $d_1 = 0$.

To study the oscillating flow in intrathecal space (the space between two concentric wavy cylinders) when mean curvature effects are consistently neglected over gap variations, we consider the case of periodic boundary conditions in the $Y$ direction. In the $X$ direction, a mean pressure gradient is imposed. In this configuration, we consider two sets of boundary conditions. With the first one, a uniformly varying pressure field $\tilde{P}_0 = X/2\pi$ on a $[0, 2\pi] \times [0, 2\pi]$ domain is imposed in the $X$ direction. The leading pressure is written as

$$\tilde{p}_0 = \tilde{p}_0' + \tilde{P}_0, \tag{4.4}$$

where $\tilde{p}'$, $z_1$ and $z_2$ are $(X, Y)$ $2\pi$-periodic function. In terms of amplitude, the boundary conditions at each order verify

$$\mathscr{P}: \quad \tilde{p}_i'(0, Y) = \tilde{p}_i'(2\pi, Y), \tag{4.5a}$$

$$\mathscr{P}: \quad \tilde{p}_i'(X, 0) = \tilde{p}_i'(X, 2\pi), \tag{4.5b}$$

for $i = 0, 1$. Alternatively, the second set of boundary conditions corresponding to imposed pressure amplitudes at $X = 0$ and $X = 2\pi$ can be considered. The resulting boundary conditions become

$$\mathscr{D}: \quad \tilde{p}_i(0, Y) = \tilde{p}_i(2\pi, Y) - d_i = 0, \tag{4.6a}$$

$$\mathscr{P}: \quad \tilde{p}_i(X, 0) = \tilde{p}_i(X, 2\pi), \tag{4.6b}$$

where $i=0,1$, $d_0=1$ and $d_1=0$. Boundary conditions $\mathscr{P}/\mathscr{P}$ (4.5) and $\mathscr{D}/\mathscr{P}$ (4.6) are both interesting to consider for CSL oscillations in intrathecal space.

Hence, three types of boundary conditions $\mathscr{D}/\mathscr{N}$, $\mathscr{P}/\mathscr{P}$ or $\mathscr{D}/\mathscr{P}$ are used in what follows.

### 4.2. *Solving the pressure Poisson problems*

With $\mathscr{D}/\mathscr{N}$ (4.3) or $\mathscr{D}/\mathscr{P}$ (4.6) boundary conditions, the leading-order pressure $\tilde{p}_0$ solves the two-dimensional Poisson problem

$$\nabla\cdot K_0(x,y)\nabla\tilde{p}_0=0. \tag{4.7}$$

When using periodic boundary conditions $\mathscr{P}/\mathscr{P}$, we must compute $\tilde{p}_0'=\tilde{p}_0-P_0$, which is the solution of

$$\nabla\cdot K_0(x,y)\nabla\tilde{p}_0'=-\nabla\cdot K_0\nabla P_0=-\frac{\partial K_0}{\partial X}\frac{1}{2\pi}. \tag{4.8}$$

At the next order, relations (4.1) can be recast into the general form

$$\nabla\cdot K_i(x,y)\nabla\tilde{p}_i=\nabla\cdot\boldsymbol{b}_i, \tag{4.9}$$

with $i=1s,1u$, $K_{1s}(x,y)=2z_-^3/3$ and $K_{1u}$ given by relation (3.20). The right-hand side is

$$\boldsymbol{b}_{1s}=G_{2s}\nabla\left(\nabla\tilde{p}_0\cdot\nabla\tilde{p}_0^*\right)+\left((G_{3s}+G_{4s})\nabla\tilde{p}_0^*\cdot(\nabla\tilde{p}_0\cdot\nabla z_-)+\text{c.c.}\right), \tag{4.10a}$$

$$\boldsymbol{b}_{1u}=G_{2u}\nabla(\nabla\tilde{p}_0)^2+(G_{3u}+G_{4u})\nabla\tilde{p}_0(\nabla\tilde{p}_0\cdot\nabla z_-), \tag{4.10b}$$

where $G_{is}$ and $G_{iu}$ $(i=2,3,4)$ are nonlinear functions of the gap space $z_-(X,Y)$ and of the Womersley number through relations (3.16) and (3.20). The right-hand side of (4.9) is a fourth-order differential operator and motivates the use of a high-order method. We discretize (4.7), (4.8) and (4.9) with a spectral method and use a variational formulation. When $\mathscr{D}/\mathscr{N}$ boundary conditions are considered, the fields are expressed as tensor products of Lagrange polynomials based on the Gauss–Lobatto–Legendre quadrature points. When periodic boundary conditions hold in one or two directions ($\mathscr{P}/\mathscr{P}$ or $\mathscr{D}/\mathscr{P}$), a Fourier basis and equally spaced points in the corresponding directions are used. In any case, the fields are represented with their values at the $(N_x+1)\times(N_y+1)$ nodes. The linear system arising from the discretization is inverted with a bi-conjugate gradient method modified to handle linear systems in which the unknowns are complex.

### 4.3. *Determination of the flow, the flux and the stream function*

Once the pressure field is known, the velocity $\boldsymbol{u}$ is obtained directly from expressions (3.7), (3.14) and (3.18) and the flux $\boldsymbol{q}$ from expressions (3.8), (3.15) and (3.19). Since the flux is divergence-free, we define the instantaneous stream function $\Psi=(0,0,\psi)$ as the solution of

$$\frac{\partial\psi}{\partial Y}=q_X,\ \frac{\partial\psi}{\partial X}=-q_Y, \tag{4.11}$$

everywhere. This problem is discretized using Gauss–Lobatto–Legendre nodes and inverted with a direct method, namely a successive diagonalization method.

For a deeper insight into inertial effects, the stream function can easily be separated into three contributions as

$$\psi(t)=\Re\{\tilde{\psi}_0\,\mathrm{e}^{\mathrm{i}t}\}+\frac{\epsilon Re}{2}(\psi_{1s}+\Re\{\tilde{\psi}_{1u}\,\mathrm{e}^{2\mathrm{i}t}\}). \tag{4.12}$$

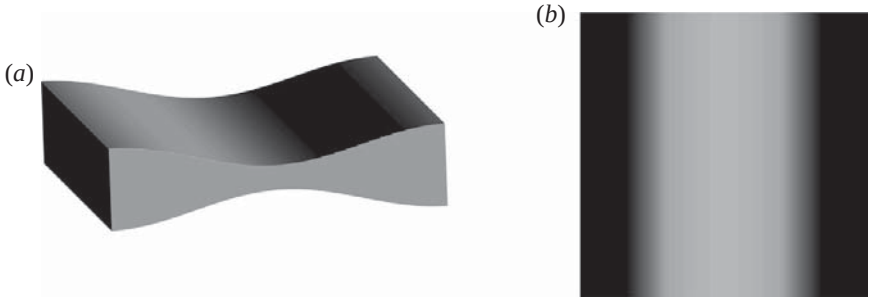


FIGURE 2. Illustration of the gap variations $z_-$ given in (5.1) in perspective view for ($a$) and with greyscale variations (identically scaled) in the $(X, Y)$ plane in ($b$). The amplitude is $\sigma = 7/13$ as used in Nishimura *et al.* (1989).

Each instantaneous stream function $\tilde{\psi}_0$, $\psi_{1s}$ and $\tilde{\psi}_{1u}$ verifies a relation of the form (4.11) that is obtained by replacing the flux with the corresponding contribution (3.8), (3.15) or (3.19), respectively. Apart from the steady-streaming stationary component $\psi_{1s}$, the instantaneous stream function $\psi$ is in no way directly related to the Lagrangian flow trajectories. Nevertheless, stream function contours provide a way of visualizing the flux $\boldsymbol{q}$, rendering its calculation worthwhile.

## 5. Numerical results

This section illustrates the intricate effect of weak inertia, Womersley number and geometrical complexity of the flow in confined wavy cavities.

### 5.1. *Two-dimensional configurations*

We first consider two-dimensional surface variations in order to compare our asymptotic analysis with previous contributions. For this, we consider a single mode variation of the gap similar to those used by Nishimura *et al.* (1989) and Sobey (1980*a*,*b*), and illustrated in figure 2:

$$z_-(X, Y) = \tfrac{1}{2}\,(1 + \sigma \cos(X)). \tag{5.1}$$

It is important to stress that the aspect ratio of the average gap to the chosen wavelength is not asymptotically small in these previous studies (e.g. $\epsilon \sim 0.4$), thus the analysis developed in this work can only be qualitative in comparison. Nevertheless, neither the numerical study conducted by Sobey (1980*a*) nor the experimental investigation (Sobey 1980*b*) provide an analysis of the steady-streaming component of the flow. Nishimura *et al.* (1989) do, however, give a qualitative representation of the steady-streaming flow patterns in the particular case of $\epsilon \simeq (2\pi)3/14$ and $\sigma = 7/13$. Figure 3 shows the streamlines in the $(X, Z)$ plane (where $Z$ refers to the unscaled vertical coordinate) associated with the two-dimensional steady-streaming flow field $(u, w)_{1s}$ ($v = 0$ in this case). For low Womersley numbers, the steady-streaming flow field displays a symmetrical quadrupolar vortex structure, the stagnation point of which is placed exactly along the longitudinal position where the depth of the channel is minimum, as shown in figure 3(*a*,*b*). Furthermore, as found in Nishimura *et al.* (1989), there is a threshold, associated to a critical Womersley number above which the flow appears, for which the flow field suddenly displays a supplementary central eddy which expands rapidly for increasing Womersley numbers, as illustrated in figure 3(*c*,*d*). This flow structure is exactly the same as that discussed in

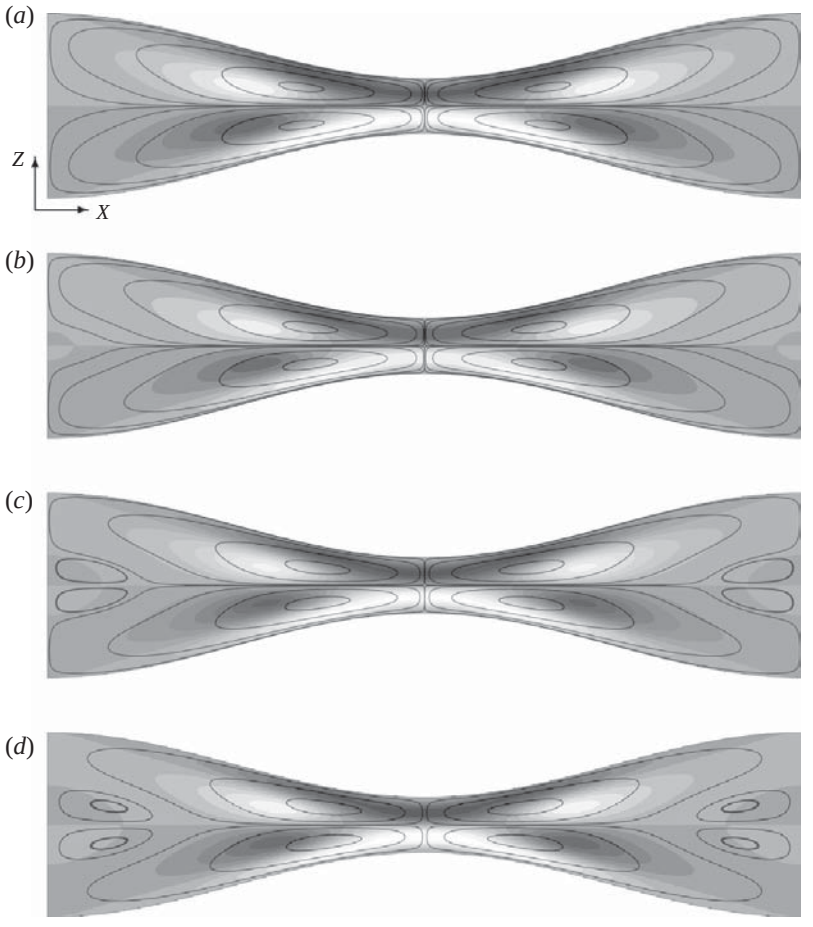


FIGURE 3. Steady-streaming streamlines in continuous lines and vertical velocity field $w_{1s}$ in greyscale for various Womersley numbers $\alpha$. The gap configuration is the one represented in figure 2(*a*,*b*) using periodic boundary conditions $\mathscr{P}/\mathscr{P}$ (4.5). (*a*) $\alpha = 12$, (*b*) $\alpha = 13$, (*c*) $\alpha = 14$, (*d*) $\alpha = 15$.

Nishimura *et al.* (1989). We found a critical Womersley $\alpha_c = 13.5$ for the central eddy apparition which differs moderately from that obtained in Nishimura *et al.* (1989), $\alpha_c \simeq 17$ (transposing their parameter definition to ours). The 20 % difference obtained can be attributed to the finite aspect ratio $\epsilon = (2\pi)3/14 \simeq (2\pi)0.21$ of their geometry, which is not that small.

### 5.2. *Three-dimensional configurations*

#### 5.2.1. *Analysis of the flow field*

Let us first choose a general family of gap variations in the $(X, Y)$ plane with a unique spatial wavelength in both directions,

$$z_{-}(X, Y) = \frac{1}{2}\left(1 + \sigma \frac{C_A \cos(X + Y) + C_B \cos(X - Y)}{C_A + C_B}\right), \tag{5.2}$$

where $C_A \geqslant 0$ and $C_B \geqslant 0$. These parameters permit the position of the bump to be varied in the $(X, Y)$ plane and $\sigma$ is the amplitude of the variation, which can be of order 1. Examples of geometries are shown in figure 4. On the numerical side,

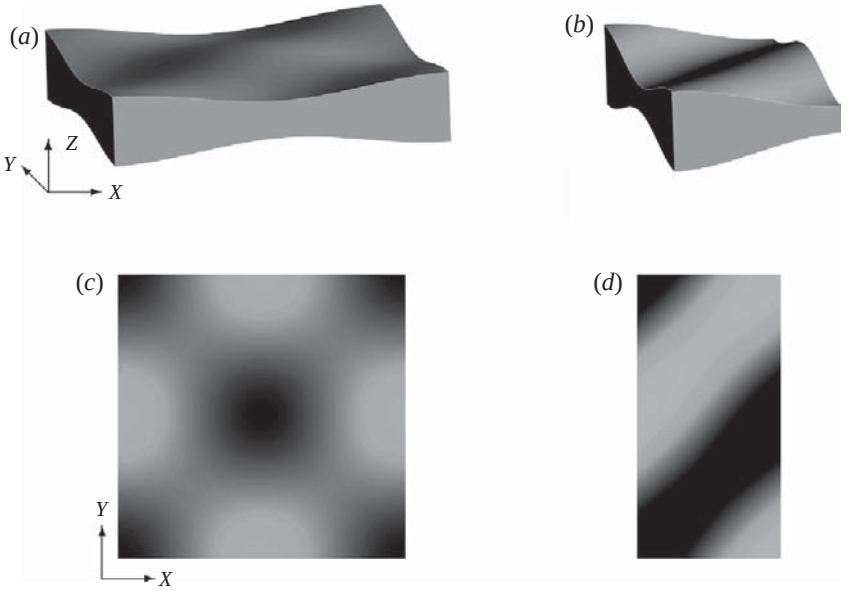


FIGURE 4. Illustration of the gap variations $z_-$ given in (5.2) in perspective view for ($a$,$b$) and with greyscale variations (identically scaled) in the $(X, Y)$ plane in ($c$,$d$). In subsets ($a$,$c$) $X, Y$ is within $[0, 2\pi]^2$, and symmetrical parameters $C_A = C_B = 1$ are chosen with a moderate amplitude $\sigma = 0.3$. In subsets ($b$–$d$) $X, Y$ is within $[0, \pi] \times [0, 2\pi]$, and highly non-symmetrical parameters $C_A = 1$, $C_B = 10$ are chosen with a more pronounced amplitude $\sigma = 0.5$.

solving configurations for which $\sigma \approx 1$ is difficult, mainly because $z_-$ approaches zero, inducing singularities in functions $G_i$ (defined in (3.16) and (3.20)). With 256 nodes in each direction, it was possible to find accurate solutions for values as high as $\sigma = 0.7$.

Before discussing the results, we summarize the symmetry properties of the lubrication equations and boundary conditions that will help us to understand the effect of the inertial nonlinearities. We first consider the case where $C_A = C_B$ (figures 4$a$,$c$) with $\mathscr{D}/\mathscr{N}$ boundary conditions. It is easy to show that the equations of the lubrication approximation with their corresponding boundary conditions are invariant under the reflections $S_X$ and $S_Y$, with respect to $X = \pi$ and $Y = \pi$ defined by

$$S_X : (X, Y) \longrightarrow (2\pi - X, Y), \qquad (\tilde{p}_0', q_{0_X}, q_{0_Y}, \psi_0) \longrightarrow (-\tilde{p}_0', q_{0_X}, -q_{0_Y}, \psi_0), \quad (5.3)$$

$$S_Y : (X, Y) \longrightarrow (X, 2\pi - Y), \qquad (\tilde{p}_0', q_{0_X}, q_{0_Y}, \psi_0) \longrightarrow (\tilde{p}_0', q_{0_X}, -q_{0_Y}, -\psi_0), \quad (5.4)$$

where $\tilde{p}_0' = \tilde{p}_0 - X/2\pi$ and $\boldsymbol{q}_0 = (q_{0_X}, q_{0_Y})$. The invariance of $z_-$ with respect to $S_X$ and $S_Y$ is of course partially responsible for these symmetry properties. Note that this invariance is preserved for $\mathscr{D}/\mathscr{N}$ boundary conditions and $\mathscr{P}/\mathscr{P}$ boundary conditions when $\tilde{p}_0'$ is replaced by $\tilde{p}_0$. Figure 5 presents the flow structure of the leading- and first-order inertial approximation at a given instant and for different Womersley numbers $\alpha = 1$, 3 and 6. As expected, the lubrication stream function $\tilde{\psi}_0$ is $S_X$- and $S_Y$-invariant (note that the stream function changes sign across the line $Y = \pi$). Figure 5 also shows that the inertial terms preserve the $S_Y$-invariance but break the $S_X$-invariance. This $S_X$-reflection invariance of $\tilde{\psi}_0$ is related to the Stokes reversibility of the streamlines. The loss of this symmetry is stronger for small $\alpha$ (compare $\alpha = 1$ in figure 5$a$,$b$ with $\alpha = 6$ in figure 5$e$,$f$). Figures 6 and 7 describe the flow structure of the steady and time-dependent corrections to the lubrication stream function. The loss of

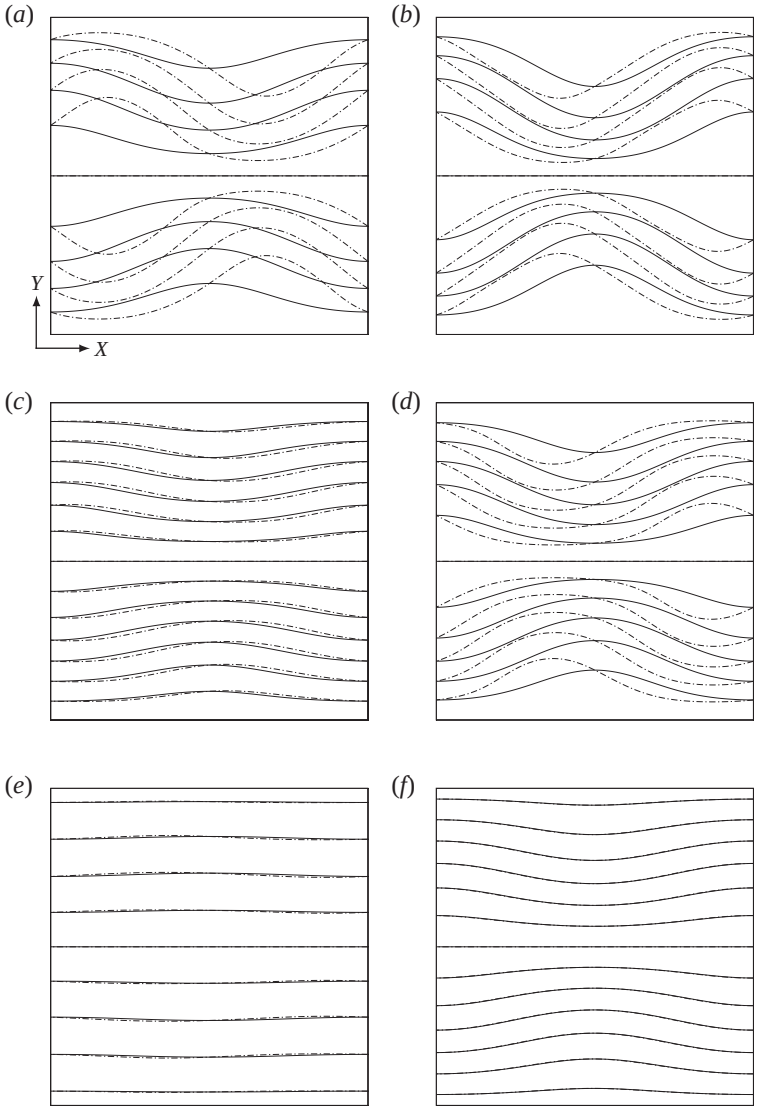


FIGURE 5. Comparison between the instantaneous complete stream function $\tilde{\psi} = \tilde{\psi}_0 + \epsilon Re\, \tilde{\psi}_1$ in dash-dotted lines and the lubrication non-inertial contribution $\tilde{\psi}_0$ in continuous lines for various Womersley numbers $\alpha = 1, 3, 6$. The gap configuration is the one represented in figure 4(*a*,*c*) using periodic boundary conditions $\mathscr{P}/\mathscr{P}$ (4.5). (*a*) $\tilde{\psi}(t=0)$ and $\tilde{\psi}_0(t=0) = \Re\{\tilde{\psi}_0\}$, $\alpha = 1$. (*b*) $\tilde{\psi}(t=3\pi/4)$ and $\tilde{\psi}_0(t=3\pi/4) = \Im\{\tilde{\psi}_0\}$, $\alpha = 1$. (*c*) Same as (*a*) for $\alpha = 3$. (*d*) Same as (*b*) for $\alpha = 3$. (*e*) Same as (*a*) for $\alpha = 6$. (*f*) Same as (*b*) for $\alpha = 6$.

the $S_X$-invariance is produced by the $S_X$-antisymmetry of the steady-streaming and pulsating inertial corrections. Figures 6 and 7 show that nonlinearities produce higher spatial harmonics than those originally present in the lubrication and aperture fields. This is more visible in figures 6(*d*) and 7(*d*), where second harmonic spatial structures now occur. Whether these higher harmonics dominate the original variations depends on the Womersley number. Figure 6 shows that a maximum is reached at a value close to $\alpha = 3$.

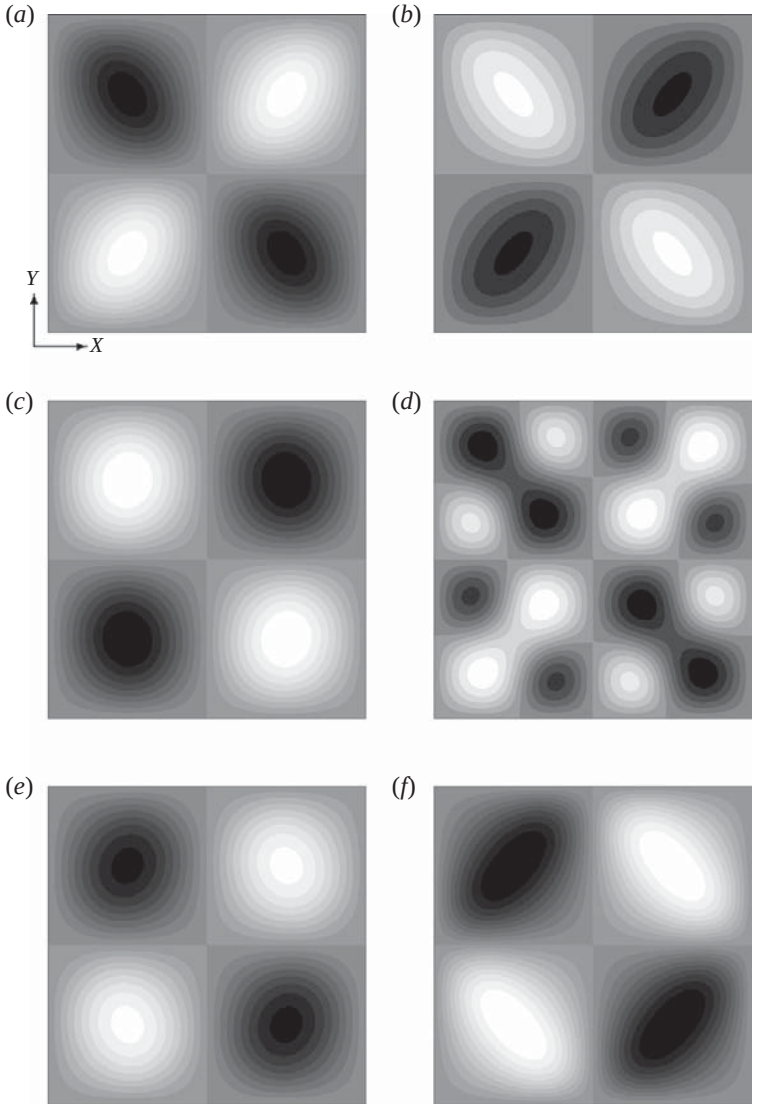


FIGURE 6. Pulsating inertial corrections $\tilde{\psi}_{1u}$ represented in greyscale for various Womersley numbers $\alpha$. The gap configuration is the one represented in figure 4(*a*,*c*) using periodic boundary conditions $\mathscr{P}/\mathscr{P}$ (4.5). (*a*) $\Re\{\tilde{\psi}_{1u}\}$, $\alpha = 1$; (*b*) $\Im\{\tilde{\psi}_{1u}\}$, $\alpha = 1$; (*c*) $\Re\{\tilde{\psi}_{1u}\}$, $\alpha = 3$; (*d*) $\Im\{\tilde{\psi}_{1u}\}$, $\alpha = 3$; (*e*) $\Re\{\tilde{\psi}_{1u}\}$, $\alpha = 6$; (*f*) $\Im\{\tilde{\psi}_{1u}\}$, $\alpha = 6$.

The relation between the flow structure and the aperture field is given in figure 8. Figure 8(*a*) shows that at small amplitude, only a single quadrupolar spatial mode exists. This suggests that the small amplitude 'weak disorder' expansion performed in Lo Jacono *et al.* (2005) for small $\sigma$ in the stationary limit $\alpha = 0$ should also be correct here for any $\alpha$. When the amplitude of the aperture variations increases (figure 8*a–d*), second spatial harmonics complexify the flow and deform the quadratic shape of figure 8(*a*) into the elongated elliptic shape of figure 8(*d*).

Let us now examine more complex configurations for which the geometry variations are associated with several spatial modes. First, we examine the situation for which

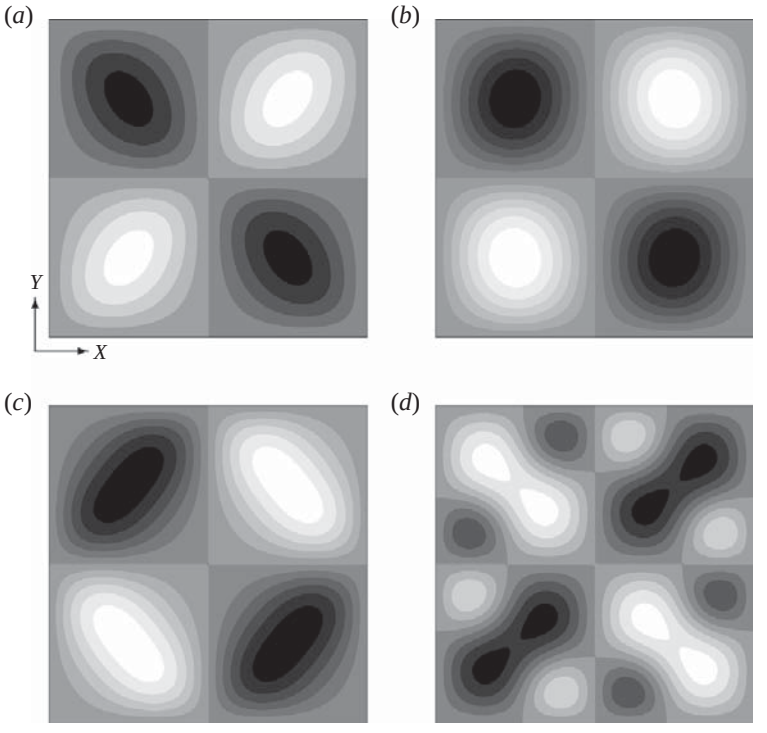


FIGURE 7. Steady-streaming corrections $\psi_{1s}$ represented in greyscale for various Womersley numbers $\alpha$. The gap configuration is the one represented in figure 4(*a*,*c*) using periodic boundary conditions $\mathscr{P}/\mathscr{P}$ (4.5). (*a*) $\alpha = 1$, (*b*) $\alpha = 3$, (*c*) $\alpha = 6$, (*d*) $\alpha = 9$.

one mode is present along the longitudinal direction whilst its wavelength doubles along the transverse one:

$$z_{-}(X, Y) = \tfrac{1}{2}[1 + 0.3\,(\cos(X + 2Y) + \cos(X - 2Y))]. \tag{5.5}$$

The cavity associated with the gap variations given in (5.5) is represented in figure 9. The resulting steady streaming is also shown in figure 10. A comparison between figures 7 and 10 obtained with the same amplitude $\sigma = 0.3$ and identical Womersley numbers indicates that the presence of higher modes in the cavity's transverse direction directly impacts the steady-streaming flow. A period doubling of the quadrupolar vortex structure is observed in the $Y$ direction in figure 10 whilst the flow evolution with the Womersley number is very similar. We now turn to cavities having two harmonic contributions in both the $X$ and $Y$ directions, illustrated in figure 11:

$$z_{-}(X, Y) = \tfrac{1}{2}(1+0.3(\cos(X+Y)+\cos(X-Y))+\tfrac{1}{5}(\cos 2(X+Y)+\cos 2(X-Y))). \tag{5.6}$$

In the case of the cavity associated with (5.6) we again used $256 \times 256$ grid points in order to be able to capture the highest modes resulting from nonlinearities. We found that the resulting steady streaming is more sensitive to the presence of higher spatial modes for some Womersley numbers than for others. The comparison between figure 7(*a*,*b*) and figure 12(*a*,*b*) does not reveal any significant differences whilst, in contrast, the harmonics shown in figure 7(*d*) are blurred in figure 12(*d*) due to some destructive interaction with the cavity's harmonics.

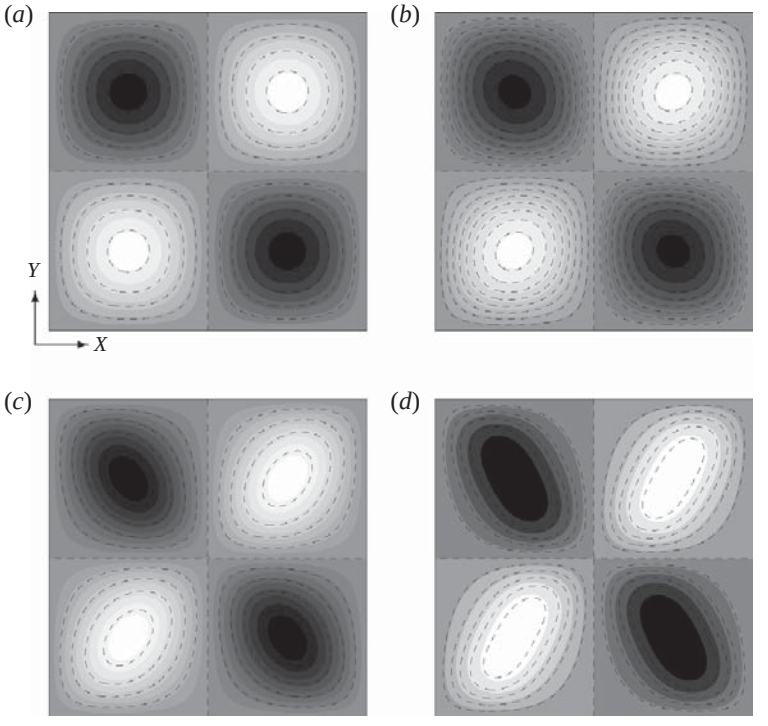


FIGURE 8. Inertial correction to the stream function when varying the amplitude parameter of the wavy confined channel $\sigma$ for a Womersley number $\alpha = 1$. The in-phase component of the double-frequency oscillating stream function $\Re\{\tilde{\psi}_{1u}\}$ is represented in greyscale while the steady-streaming component $\psi_{1s}$ is shown with dashed lines. (*a*) $\sigma = 0.0005$, (*b*) $\sigma = 0.1$, (*c*) $\sigma = 0.3$, (*d*) $\sigma = 0.5$.

### 5.2.2. *Pressure–flux relationship*

At the leading order, the linear relation between the pressure and the flux produces a complex hydraulic conductance that depends on the Womersley number and cavity shape. At the next order, conditions are investigated in which a persistent non-zero time average flux is induced by nonlinear inertial effects. In this subsection, we seek a general expression for the dimensionless flux $Q(\Delta p)$ defined in (3.3), of the form

$$Q = \Re\{\tilde{C}_0 \, \mathrm{e}^{\mathrm{i}t}\}\Delta p + \frac{\epsilon Re}{2}(C_{1s} + \Re\{\tilde{C}_{1u} \, \mathrm{e}^{2\mathrm{i}t}\})\Delta p^2, \tag{5.7}$$

where $\Delta p$ is the dimensionless pressure difference.

### 5.2.3. *Lubrication hydraulic conductance*

The first term on the right-hand side of (5.7) is the lubrication contribution of the complex total hydraulic conductance $\tilde{C}_0$ of the flow. As a result of the in-phase applied pressure $\Delta P \mathrm{e}^{\mathrm{i}t}$, there is either an in-phase response of the flux associated with $\Re\{\tilde{C}_0\}$ or an out-of-phase response associated with $\Im\{\tilde{C}_0\}$ and physically produced by the delayed viscous response in the Stokes layers. In the case of two parallel plates, for which $\sigma = 0$ and the pressure drop $\Delta P$ is applied over a longitudinal distance $L$ along $X$ (the cavity length is not necessarily equal to the typical in-plane variations $\lambda/2\pi$ chosen as the dimensional reference length scale), $\tilde{C}_0$ is equal to $LK_0/\lambda \equiv (L/\lambda)K_0(z_- = 1/2)$. This was obtained from relation 3.8*b* evaluated at $z_- = 1/2$ which is the limit of (5.2) when $\sigma = 0$. Thus, for two parallel plates this total

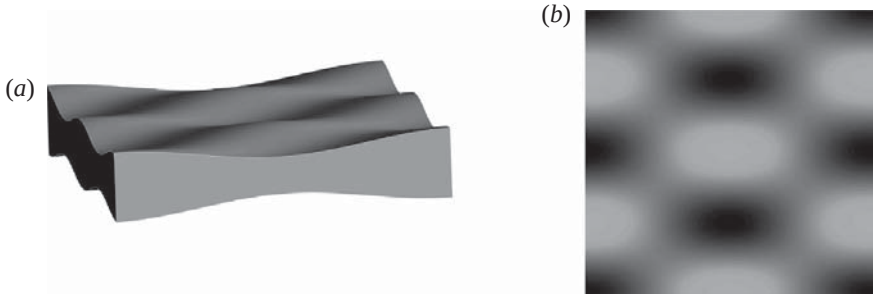


FIGURE 9. Illustration of the gap variations associated with spatial variations (5.5).

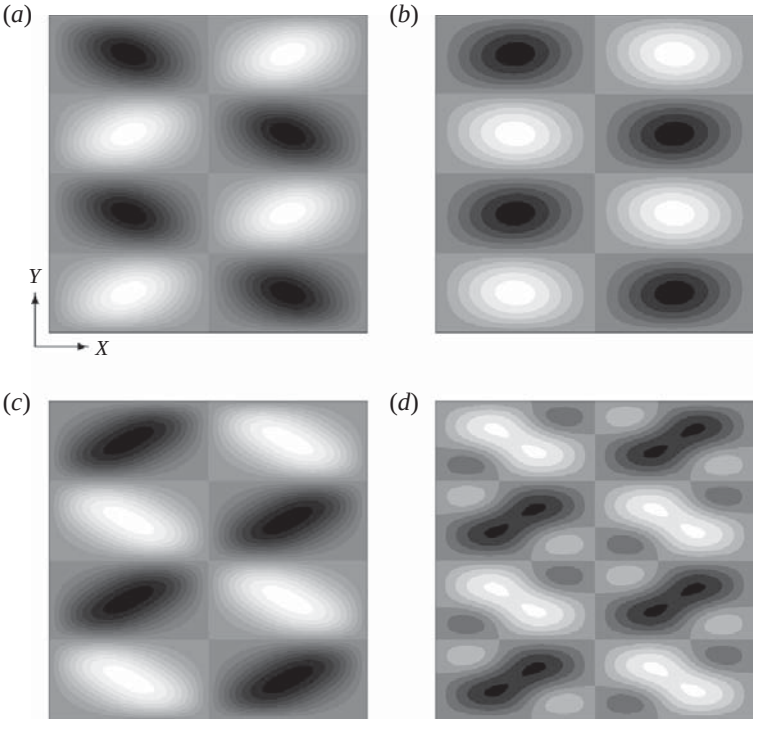


FIGURE 10. Steady-streaming corrections $\psi_{1s}$ represented in greyscale for various Womersley numbers $\alpha$. The gap configuration is the one represented in figure 9(*a*,*b*) using periodic boundary conditions $\mathscr{P}/\mathscr{P}$ (4.5). (*a*) $\alpha = 1$, (*b*) $\alpha = 3$, (*c*) $\alpha = 6$, (*d*) $\alpha = 9$.

hydraulic conductance reads

$$\tilde{C}_0 = \frac{L}{\lambda k^2}\left(1 - \frac{2}{k}\tanh\frac{k}{2}\right), \tag{5.8a}$$

$$\alpha \ll 1 \quad \tilde{C}_0 = \frac{L}{\lambda}\left(-\frac{1}{12} - \mathrm{i}\frac{\alpha^2}{120} + \cdots\right), \tag{5.8b}$$

$$\alpha \gg 1 \quad \tilde{C}_0 = \frac{L}{\lambda}\left(-\frac{\mathrm{i}}{\alpha^2} + (1+\mathrm{i})\frac{\sqrt{2}}{\alpha^3} + \cdots\right), \tag{5.8c}$$

where (5.8*b*) and (5.8*c*) are the small and large Womersley limit of (5.8*a*). The large- or small-Womersley-number asymptotic behaviour given in (5.8*b*,*c*) is shown

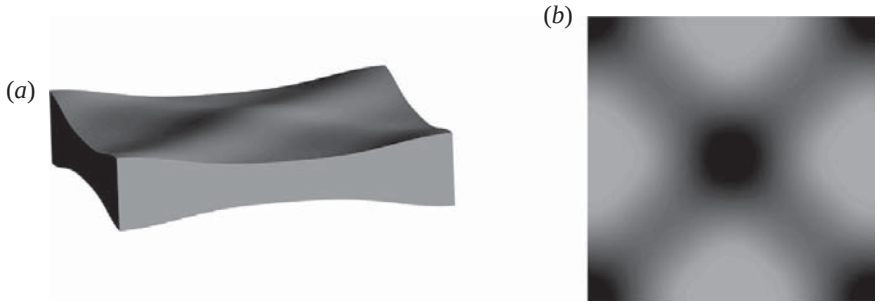


FIGURE 11. Illustration of the gap variations associated with spatial variations (5.6).

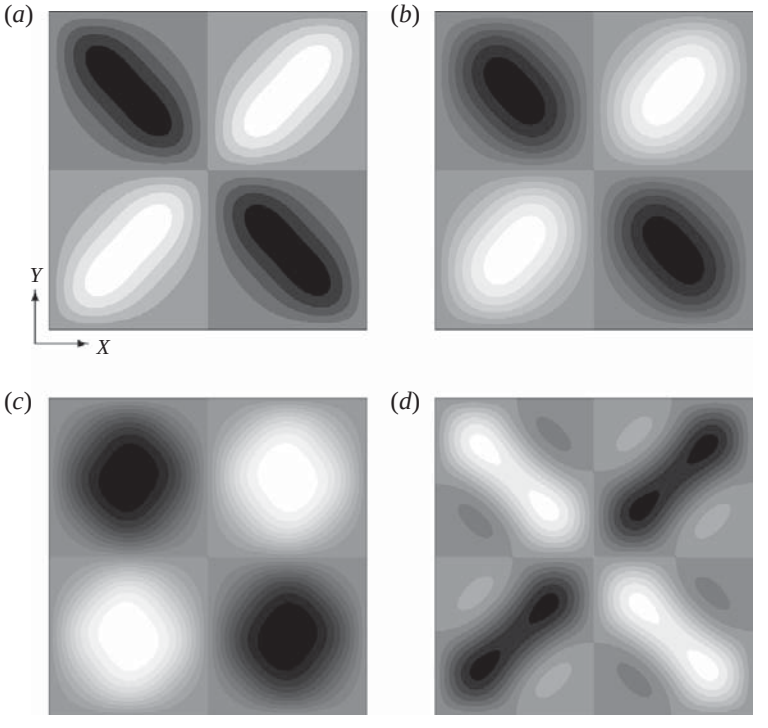


FIGURE 12. Steady-streaming corrections $\psi_{1s}$ represented in greyscale for various Womersley numbers $\alpha$. The gap configuration is the one represented in figure 11(*a*,*b*) using periodic boundary conditions $\mathscr{P}/\mathscr{P}$ (4.5). (*a*) $\alpha = 1$, (*b*) $\alpha = 3$, (*c*) $\alpha = 6$, (*d*) $\alpha = 9$.

for easier comparison with the results in a non-parallel cavity. In the case of the variable aperture field of figure 4(*a*,*c*), whose longitudinal length is $L = \lambda$ so that the dimensionless cavity longitudinal size is $2\pi$, the variations of $\tilde{C}_0$ are reported in figure 13(*a*). It follows the same algebraic dependence on $\alpha$ as (5.8), but with different prefactors which depend on the aperture $z_-$ through parameters $C_A, C_B$ and the amplitude $\sigma$. Figure 13(*a*) does not reveal any great difference between the asymptotic behaviour of the parallel plate configuration (5.8) and the hydraulic conductance $\tilde{C}_0$ found in the case $C_A = C_B = 1$, $\sigma = 0.3$. This is due to the prefactors correcting the parallel case, which are of order $O(\sigma^2)$ and therefore smaller than the order-1 prefactors of (5.8). Neither the real nor the imaginary part changes sign with the Womersley number: there is obviously no backflow to the applied pressure drop.

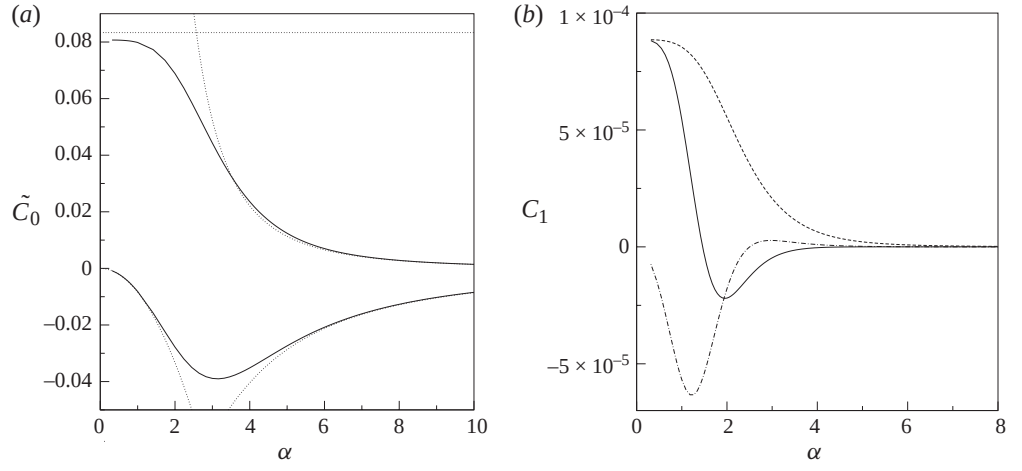


FIGURE 13. Hydraulic conductances for lubrication leading order in (*a*) and quadratic inertial corrections in (*b*). (*a*) The gap variations represented in figure 4(*a,c*) were chosen. $\Re\{\tilde{C}_0\}$ is the upper continuous curve and $\Im\{\tilde{C}_0\}$ is the lower continuous one. Dotted lines show the asymptotic behaviour of the homogeneous case (5.8). (*b*) The gap variations represented in figure 4(*b,d*) were chosen with $\mathscr{D}/\mathscr{N}$ boundary conditions (4.2). $\Re\{C_{1u}\}$ is the continuous curve and $\Im\{C_{1u}\}$ is the lower dash-dotted line. The steady-streaming contribution $C_{1s}$ is also represented by a dashed line.

Furthermore, it is interesting to note that the 'inductive effects' associated with $\Im\{\tilde{C}_0\}$ are maximal for an intermediate Womersley number close to 3. For larger values, $\Re\{\tilde{C}_0\}$ decays as $\sim 1/\alpha^3$ whilst $\Im\{\tilde{C}_0\}$ decays as $\sim 1/\alpha^2$, as expected (Leal 1992).

Figure 13(*a*) also investigates the effect of the boundary conditions on the hydraulic conductance $\tilde{C}_0$ for the aperture field illustrated in figure 4(*a,c*). The boundary conditions $\mathscr{P}/\mathscr{P}$ (4.5) or $\mathscr{D}/\mathscr{P}$ (4.6) did not produce conductances that differed significantly from each other.

### 5.2.4. *Inertial hydraulic conductances*

We next investigate the possible contribution of nonlinear effects to the second and third terms of the right-hand side terms of relation (5.7), although such effects do not occur in many configurations. For periodic lateral boundary conditions $\mathscr{P}/\mathscr{P}$ (4.5) and $\mathscr{D}/\mathscr{P}$ (4.6), we find that $C_{1s}$ and $\tilde{C}_{1u}$ are both zero for any $z_-$ of the form (5.2). More precisely, with these configurations, for any parameter $C_A$, $C_B$ or $\sigma$, we obtained $C_{1s} = \tilde{C}_{1u} = 0$. A similar result was also obtained at the stationary limit by Lo Jacono *et al.* (2005). This is reminiscent of what has already been found in porous media by Mei & Auriault (1991), namely that homogeneous micropore geometry has zero quadratic macroscopic inertial corrections. This theoretical result led to a number of discussions in the porous media research community because most experimental observations reported the opposite, i.e. a quadratic correction. It was finally discovered by Firdaouss, Guermond & Le Quéré (1997) that some quadratic corrections could be obtained if some disorder was introduced at the pore scale or if finite size effects (non-converged statistical averages) were considered.

In the present situation, we investigate the possibility of quadratic effects occurring in a finite-sized cavity. With $\mathscr{D}/\mathscr{N}$ (4.3) boundary conditions and a domain bounded in the transverse reflection, these nonlinear effects may make a non-zero contribution to the flux, provided that the flow breaks the transverse reflection invariance $S_Y$. We

found numerically that the magnitude of this contribution depended on how much the symmetry was broken: it increased with the departure from the $S_Y$-invariant case. This effect with the geometries is sketched in figure 4(*b*,*d*) using $C_A = 1$ and $C_B = 10$. Figure 13(*b*) represents the inertia hydraulic conductances $C_{1s}$ and $\tilde{C}_{1u}$ of the steady-streaming and oscillating terms, respectively. Their variations are of the same order of magnitude but three orders smaller than the leading order $\tilde{C}_0$.

The steady-streaming component nevertheless represents the only time-averaged non-zero contribution to the flux (5.7). Hence, although small, it is the only systematic continuous out-going flux associated with the applied pulsating pressure drop. The existence of non-zero $C_{1s}$ reflects the symmetry breaking of the steady-streaming flow along the longitudinal direction. The variation of $C_{1s}$ in figure 13(*b*) shows a uniform decay as Womersley number increases, associated with the shrinkage of the thickness of the Stokes layers. Hence, from the interplay of nonlinear effects and broken symmetries, some continuous fluxes can be driven out of a wavy cavity of finite size.

## 6. Discussion and conclusion

### 6.1. *Discussion*

This section reviews the limitations and possible extensions of the proposed analysis. First, since our analysis relies heavily on the lubrication approximation, many complex flow patterns found in large-amplitude geometries cannot be captured in this special limit. More precisely, we consider the dimensionless amplitude $\sigma \sim O(1)$, but the lubrication approximation breaks down when $\sigma \sim O(1/\epsilon)$ or $\epsilon \sim O(1)$. For example, in the case of varicose shape variation considered in this study, it is clear that the filling vortex found in short-wavelength transversely invariant furrowed channels in Sobey (1980*a*,*b*) cannot be captured. In particular, the vortices found for sinusoidal channel shapes are already present at zero Reynolds number and are reminiscent of Moffat's eddies. They appear when the ratio between the mean channel depth and the wavelength is close to $\epsilon = (2\pi)0.8$ (Pozrikidis 1987) in the limit $\alpha = 0$. Nevertheless, when considering the influence of inertial effects (see § 5), we found a flow pattern of transverse steady-streaming vortices qualitatively similar to those found for a finite aspect ratio. These results qualitatively explain the experimental results found in Nishimura *et al.* (1989) and Sobey (1980*b*), where it is shown that central eddies are inertially driven.

Furthermore, interesting effects associated with sinuous variations are not present in this analysis. We did not *a priori* neglect or ignore the impact of sinuous effects, since any long-wavelength channel shape is indeed considered. They do affect the leading-order third component of the velocity $w_0^+$. Nevertheless, it turns out that sinuous variations do not influence the in-plane flow at the leading order, whether inertial effects are included or not, when $O(\epsilon^2)$ terms are neglected. The inclusion of $O(\epsilon^2)$ terms when taking into account the curvature terms could be a possible extension of this work, and should provide the flow influence of sinuous variations.

As mentioned previously, the analysis presented is a long-wavelength $\epsilon \ll 1$, moderate-Reynolds-number analysis $\epsilon Re \ll 1$. These hypotheses are consistent with both intrathecal space variations $h/\lambda \sim 1/10$ and Reynolds number $Re \sim 1$–$10$ evaluated from human *in vivo* measurements by Balédent *et al.* (2007). We expected the influence of inertia effects on the flow to be very weak. We have shown that, although small, inertia effects induce the only non-zero time-averaged quantities in this analysis and could be of importance. In this paper, we have investigated inertia-driven stationary flux production. It might be a possible mechanism for the CSL renewal, which is known to be drained from brain tissue to venous compartments at

very low flow rates. Some other issues associated with the convective steady-streaming transport of some drugs delivered inside the intrathecal space might also be of interest for future studies.

Although lubrication generally provides fairly robust approximations, a more quantitative estimate of the influence of either $O(\epsilon^2)$ curvature effects or mean curvature $O(h/D)$ contributions in realistic cavities should be interesting to evaluate. The moderate-Reynolds hypothesis has also previously shown intriguing robustness to values as large as $Re \sim 10/\epsilon$ for stationary conditions (Lo Jacono *et al.* 2005). A careful analysis of the discarded terms of (2.6) shows a supplementary constraint on the lower value of the Reynolds number: $Re \gg \max(\epsilon, \epsilon\alpha^2)$. The first condition is not difficult to meet, since if $Re \leqslant \epsilon$, inertial effects are negligible, and thus not interesting. The second condition can be more restrictive if $\alpha^2$ becomes very large. It should be noted that the interesting physiological range of values for CSL flow is $\alpha^2$ within 0.5–3, so the constraint on the largest Reynolds number values associated with the Womersley number $\epsilon^2\alpha^2 \ll 1$ can safely be met for $\epsilon$ ratios smaller than $1/\sqrt{3} \simeq 0.57$.

Finally, we would like to discuss the possibility of taking into account general multi-mode temporal variations in the pressure forcing in a similar analysis. The leading-order lubrication flow being linear, the flow field can be obtained easily for these more general conditions from the Fourier transform of the applied pressure temporal variations. The lubrication solution will then decompose into the linear superposition of all the Fourier modes, and it is thus easy to obtain from our analysis. Further nonlinear effects are more complicated to evaluate since linear superposition no longer applies for the forcing terms associated with the Reynolds stress. The lubrication solution enters into the Reynolds stress forcing in relations (3.13) and (3.17) through a convolution product between Fourier modes. In this analysis we have evaluated the effect of each velocity mode $\mathscr{U}_0(\alpha)$ on itself in the nonlinear Navier momentum convection term. In order to analyse more general time-dependent forcing, one should compute the effect of one mode $\mathscr{U}_0(\alpha)$ on another mode $\mathscr{U}_0(\alpha')$, which means computing the interaction between modes. It might then be possible to find the solution of inertial corrections by computing first the response to each coupled mode interaction and latter proceeding to the convolution product by summing all possible coupled contributions. A treatment similar to the one used in this manuscript should then be applied to evaluate the flow forced by Reynolds stress coupled mode interactions. This might lead to an expression similar to relations (3.14) and (3.18), which are indeed the results obtained for the cross-contribution of the same mode. Such computations would nevertheless require a non-negligible algebraic effort.

### 6.2. *Conclusion*

We have conducted a theoretical analysis of weak-inertial lubricated confined flows oscillating in a wavy open channel. We considered channels in which the variations in the two horizontal directions had long wavelengths compared with the mean vertical distance $h$ between the channel walls ($h/\lambda \ll 1$). The flow is governed by two independent dimensionless parameters: the lubricated Reynolds number $\epsilon Re$ and the Womersley number $\alpha$. We calculated the first inertial correction to the lubrication theory and obtained a complete analytical expression of the flow field dependence on both the channel transverse (vertical) direction and the Womersley number. These variations are decoupled from the spatial variations in the two other horizontal directions. The pressure problem in the horizontal coordinates has been formulated at the lubrication limit and at the first order including inertial corrections. The inertial pressure corrections are coupled to the leading-order lubrication pressure through

fourth-order nonlinear forcing terms and must be solved numerically. We show that some of the symmetry invariances of the lubricated flow are broken by inertial effects. The inertial flow correction has two distinct components: a stationary steady-streaming flow and a harmonic oscillating one. Both of them have been computed for various cavity shapes. In the case of two-dimensional transversely invariant shapes we recover previously published results on the steady-streaming quadrupolar vortex flow. We consistently found a critical Womersley number for the appearance of a central eddy. For one-mode three-dimensional cavities, we show that the steady streaming also displays a quadrupolar flow in the horizontal $(X, Y)$ plane of the cavity.

When increasing the Womersley number, this quadrupolar flow shows a transition towards an octupolar structure when the amplitude of the wall variations is sufficiently great for large Womersley numbers. When some higher harmonic variations are present in the cavity shape, they can also influence the steady streaming. We first showed that the cavity wavelength had a direct influence on the steady-streaming wavelength. Furthermore we also observed that the cavity harmonics could influence the steady-streaming harmonics at large Womersley number.

Finally, we have analysed the total flux–pressure relationship. It involves different hydraulic conductances, which have been computed. We first computed the linear conductance and analysed its asymptotic behaviour for large or small Womersley number. We found a very small influence of the applied boundary conditions for this linear conductance, in contrast to those associated with inertial contributions. For periodic boundary conditions we found zero contribution of inertial effects to the mean flux. Conversely, when breaking the channel shape symmetry and when considering Dirichlet–Neumann boundary conditions we found a non-zero inertial contribution to the mean flux. The time-averaged flux showed a non-trivial continuous contribution from the steady streaming, which could be triggered by changing the Womersley number.

We are grateful to Professor Peter Monkewitz, Professor E. J. Hinch, Dr R. Nelissen, Dr D. Lasseux and Professor M. Zagzoule for interesting discussions. This work was supported by GDR 2760, 'Biomécanique des fluides et des transferts: Interaction fluide/structure biologique', the ASUPS A05 of Paul Sabatier University, Toulouse, France and the ANR project ANR-06-BLAN-0238-01. We would also like to thank one referee for particularly thoughtful, deep and profitable insights in their correction of the manuscript.

## Appendix. Velocity field analytic expressions

$$\left.\begin{aligned}
F_{1s} &= \frac{\hat{z}^2 - z_-^2}{2},\\
F_{2s} &= \frac{1}{2k^4}\left(\frac{z_-^2 - \hat{z}^2}{2} + \frac{\sinh(kz_-)\sinh(k^*z_-) - \sinh(k\hat{z})\sinh(k^*\hat{z})}{2kk^*\cosh(kz_-)\cosh(k^*z_-)}\right.\\
&\qquad\left. + \frac{1}{k^2}\left(\frac{\cosh(k\hat{z})}{\cosh(kz_-)} - \frac{\cosh(k^*\hat{z})}{\cosh(k^*z_-)}\right)\right),\\
F_{3s} &= \frac{\tanh(k^*z_-)}{2k^4}\left(\frac{1}{k^*}\left[1 - \frac{\cosh(k^*\hat{z})}{\cosh(k^*z_-)}\right] + \frac{\sinh(k\hat{z})\sinh(k^*\hat{z}) - \sinh(kz_-)\sinh(k^*z_-)}{2k\cosh(kz_-)\cosh(k^*z_-)}\right),\\
F_{4s} &= \frac{\tanh(kz_-)}{k^3[kz_-\cosh(kz_-) - \sinh(kz_-)]}\left(\frac{\sinh(kz_-)(\hat{z}\sinh(k^*\hat{z}) - z_-\sinh(k^*z_-))}{2k^*\cosh(k^*z_-)}\right.\\
&\quad\left. + \frac{z_-}{4k}\left(\cosh(kz_-) - \frac{\cosh(k\hat{z})\cosh(k^*\hat{z})}{\cosh(k^*z_-)}\right) + \frac{\sinh(kz_-)}{k^2}\left(\frac{\cosh(k^*\hat{z})}{\cosh(k^*z_-)} - 1\right)\right).
\end{aligned}\right\} \tag{A 1}$$

$$
\left.
\begin{aligned}
F_{1u} &= \frac{1}{2k^2}\left(\frac{\cosh(\sqrt{2}k\hat{z})}{\cosh(\sqrt{2}kz_-)}-1\right),\\
F_{2u} &= \frac{1}{4k^6}\left(\left(\frac{\cosh(\sqrt{2}k\hat{z})}{\cosh(\sqrt{2}kz_-)}-1\right)\left(\frac{1}{\cosh^2(kz_-)}-4\right)+\left(\frac{\cosh(k\hat{z})}{\cosh(kz_-)}+2\right)^2-9\right),\\
F_{3u} &= \frac{\tanh(kz_-)}{2k^5}\left(\frac{\cosh(\sqrt{2}k\hat{z})}{\cosh(\sqrt{2}kz_-)}\left[3-\frac{1}{\cosh^2(kz_-)}\right]-\frac{\sinh^2(k\hat{z})}{\cosh^2(kz_-)}-\frac{2\cosh(k\hat{z})}{\cosh(kz_-)}\right),\\
F_{4u} &= \frac{\sinh(kz_-)}{k^4(kz_-\cosh(kz_-)-\sinh(kz_-))}\left(\frac{\tanh(kz_-)}{\cosh(kz_-)}(\hat{z}\sinh(k\hat{z})+\frac{2\cosh(k\hat{z})}{k}\right)\\
&\quad +\frac{z_-}{2}\frac{\cosh^2(k\hat{z})}{\cosh^2(kz_-)}+\frac{\cosh(\sqrt{2}k\hat{z})}{\cosh(\sqrt{2}kz_-)}\left[\frac{z_-}{2}\left(\frac{2}{\cosh^2(kz_-)}-3\right)-\frac{2\tanh(kz_-)}{k}\right]\Bigg).
\end{aligned}
\right\}
\tag{A 2}
$$

## REFERENCES


Balédent, O., Ambarkia, K., Kongolob, G., Bouzerara, R., Gondry-Jouetc, C. & Meyer, M. E. 2007 Cerebral flow modeling using electrical analogue: MRI velocimetry validation. *Med. Nucl.* **31** (1), 16–28.

Duck, P. W. & Smith, F. T. 1979 Steady streaming induced between oscillating cylinders. *J. Fluid Mech.* **91**, 93–110.

Firdaouss, M., Guermond, J.-L. & Le Quéré, P. 1997 Non-linear corrections to Darcy's law at low Reynolds numbers. *J. Fluid Mech.* **343**, 331–350.

Grotberg, J. B. 1984 Volume-cycled oscillatory flow in a tapered channel. *J. Fluid Mech.* **141**, 249–264.

Gupta, S., Poulikakos, D. & Kurtcuoglu, V. 2008 Analytical solution for pulsatile viscous flow in a straight elliptic annulus and application to the motion of the cerebrospinal fluid. *Phys. Fluids* **20**, 093607.

Hall, P. 1974 Unsteady viscous flow in a pipe of slowly varying cross-section. *J. Fluid Mech.* **64**, 209–226.

Leal, L. G. 1992 *Laminar Flow and Convective Transport Processes*. Butterworth–Heinemann Series in Chemical Engineering.

Lo Jacono, D., Plouraboué, F. & Bergeon, A. 2005 Weak-inertial flow between two rough surfaces. *Phys. Fluids* **17**, 063602.

Manton, M. J. 1971 Low Reynolds number flow in slowly varying axisymmetric tubes. *J. Fluid Mech.* **49**, 451–459.

Mei, C. C. & Auriault, J.-L. 1991 The effect of weak inertia on flow through a porous medium. *J. Fluid Mech.* **222**, 647–663.

Nelissen, R. M. 2008 Fluid mechanics of intrathecal drug delivery. PhD thesis, École Polytechnique Fédérale de Lausanne, Lausanne, Switzerland.

Nishimura, T., Arakawa, S., Shinichiro, M. & Kawamura, Y. 1989 Oscillatory viscous flow in symmetric wavy-walled channels. *Chem. Engng Sci.* **44**, 2137–2148.

Padmanabhan, N. & Pedley, T. J. 1987 Three-dimensional steady streaming in a uniform tube with an oscillating elliptical cross-section. *J. Fluid Mech.* **178**, 325–343.

Pozrikidis, C. 1987 Creeping flow in two-dimensional channels. *J. Fluid Mech.* **180**, 495–514.

Ralph, M. E. 1986 Oscillatory flows in wavy-walled tubes. *J. Fluid Mech.* **168**, 515–540.

Ramachandra Rao, A. & Devanathan, R. 1973 Pulsatile flow in tubes of varying cross-sections. *Z. Angew. Math. Phys.* **24**, 203–213.

Selderov, K. P. & Stone, H. A. 2001 Peristaltically driven channel flows with applications toward micromixing. *Phys. Fluids* **13**, 1837–1855.

Sobey, I. J. 1980*a* On the flow furrowed channels. Part 1. Calculated flow patterns. *J. Fluid Mech.* **96** (1), 1–26.

Sobey, I. J. 1980*b* On the flow furrowed channels. Part 2. Observed flow patterns. *J. Fluid Mech.* **96** (1), 27–32.

Sobey, I. J. 1985 Dispersion caused by separation during oscillatory flow through a furrowed channel. *Chem. Engng Sci.* **40**, 2129–2134.

Stroock, A. D., Dertinger, S. K. W., Ajdari, A., Mezić, I., Stone, H. A. & Whitesides, G. M. 2002 Chaotic mixer for microchannels. *Science* **295**, 647–651.

Waters, S. L. 2001 Solute uptake through the walls of a pulsating channel. *J. Fluid Mech.* **433**, 193–208.